Supporting Information

Completely Degradable Bilayer Functional-Ionic Wood Heterostructure-Derived Nanogenerator for Eco-Friendly Power Generation

Vishu Verma[a], Ritik Mohanty[b], Romy Garg[c] and Kaushik Parida[a,d]*

*Corresponding author

E-mail address: kaushik.parida@pe.iitr.ac.in

Note S1: Delignification of wood

Wood primarily consists of cellulose, hemicellulose, and lignin. The extraction of lignin from wood results in a cellulose-based network. Native balsa wood exhibits a yellowish colour, whereas delignified wood appears white, indicating significant lignin removal. Upon the removal of lignin and hemicelluloses, the compact cell walls became detached, leading to the merging of open spaces within the cells. Consequently, delignified wood exhibits a noticeable reduction in size along the tangential direction compared to the native wood, as shown in Figure S1.

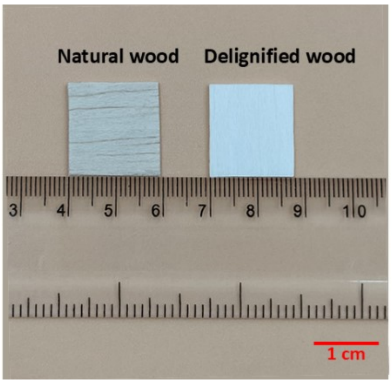

Fig. S1. Digital photograph of natural wood and delignified wood.

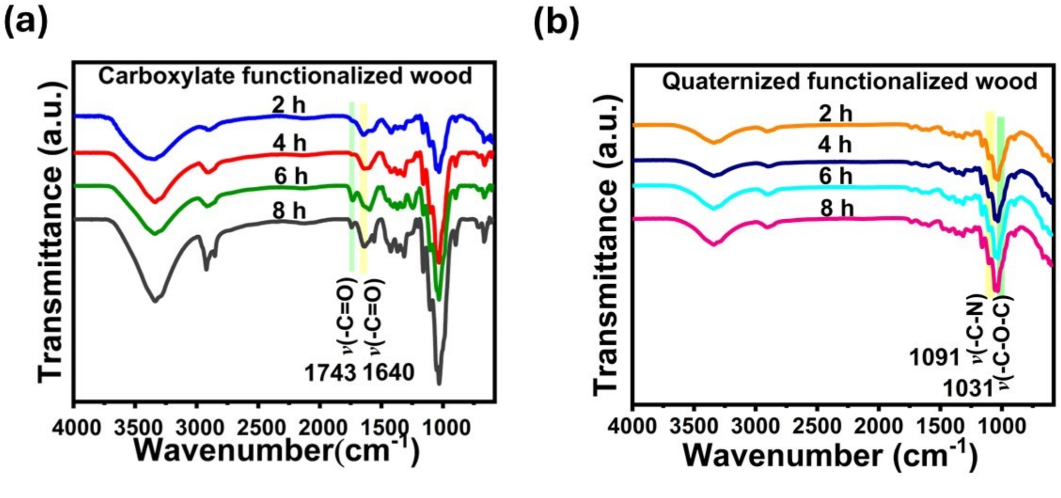

Fig. S2. FTIR spectra of (a) CFW and (b) QFW with varying amount of functionalization.

Note S2: Conductometric titration

A conductometric titration method was employed to investigate the -COOH amount (mmol g^{-1}) in carboxylate-functionalized wood. A 0.2 wt% sample solution (0.02 g in 10 ml deionised water) was prepared by dispersing carboxylate functionalized wood in deionised water using ultrasonication. The pH value of the suspension was adjusted to 3.0 by adding 1 M HCl. The conductivity of the suspension was continuously measured by a conductivity meter (Mettler Toledo, Seven Excellence Cond meter S700) as 0.1 M NaOH was dropwise added into the suspension under stirring. Fig. S3 demonstrates the relationship between conductivity and NaOH volume, enabling the calculation of carboxylate content (C_{-COOH}) using the following equation:

$$C_{-COOH} = \frac{C_{NaOH} \times (V_2 - V_1)}{W}$$

Where C_{NaOH} (molL^{-1}), (V_2-V_1)(ml) and W(g) were the concentration of NaOH, volume of NaOH neutralized by -COOH, and sample weight.

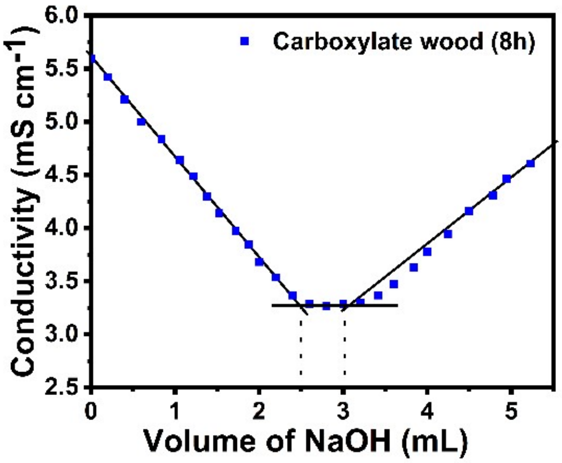

Fig. S3. Conductimetric titration curve for evaluating the -COOH content in CFW synthesized at 4h reaction duration.

Table S1. Evaluation of -COOH amount in CFW with varying reaction duration using conductometric titration.

S. No.	Time (h)	V_2-V_1 (ml)	-COOH content (mmol g^{-1})
1	2	0.15	0.7
2	4	0.33	1.6
3	6	0.45	2.2
4	8	0.75	3.7

Table S2. Nitrogen amount (%) in QFW at different reaction duration, determined via CHNS elemental analysis.

S. No.	Time (h)	-N content (%)
1	2	0.4
2	4	1.2
3	6	2.3
4	8	3.8

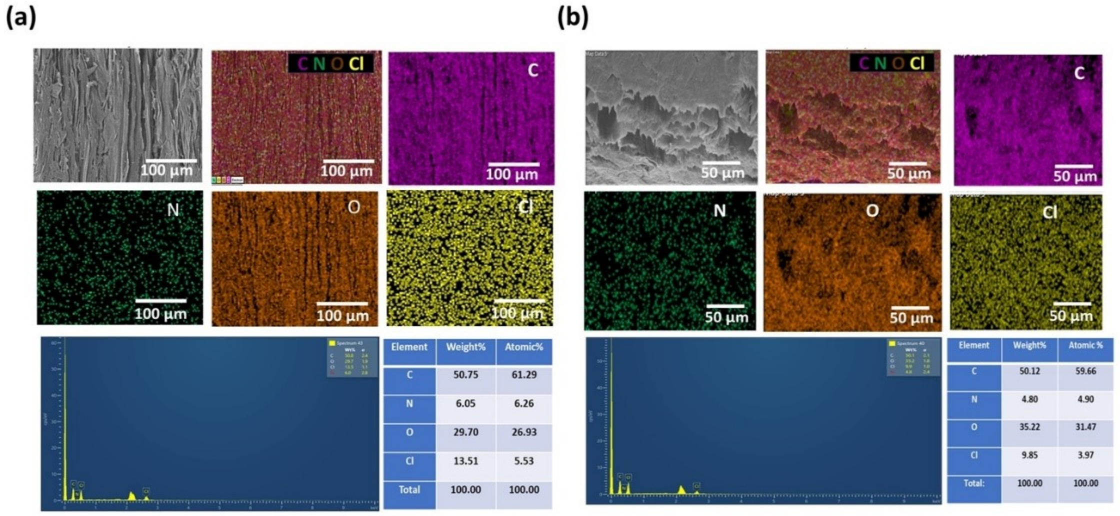

Element	Weight%	Atomic%
C	50.75	61.29
N	6.05	6.26
O	29.70	26.93
Cl	13.51	5.53
Total	100.00	100.00

Element	Weight%	Atomic%
C	50.12	59.66
N	4.80	4.90
O	35.22	31.47
Cl	9.85	3.97
Total:	100.00	100.00

Fig. S4. Element mapping images of EDX confirming the presence of nitrogen in quatern wood: (a) longitudinal view (vertical view) and (b) cross-sectional view (horizontal view).

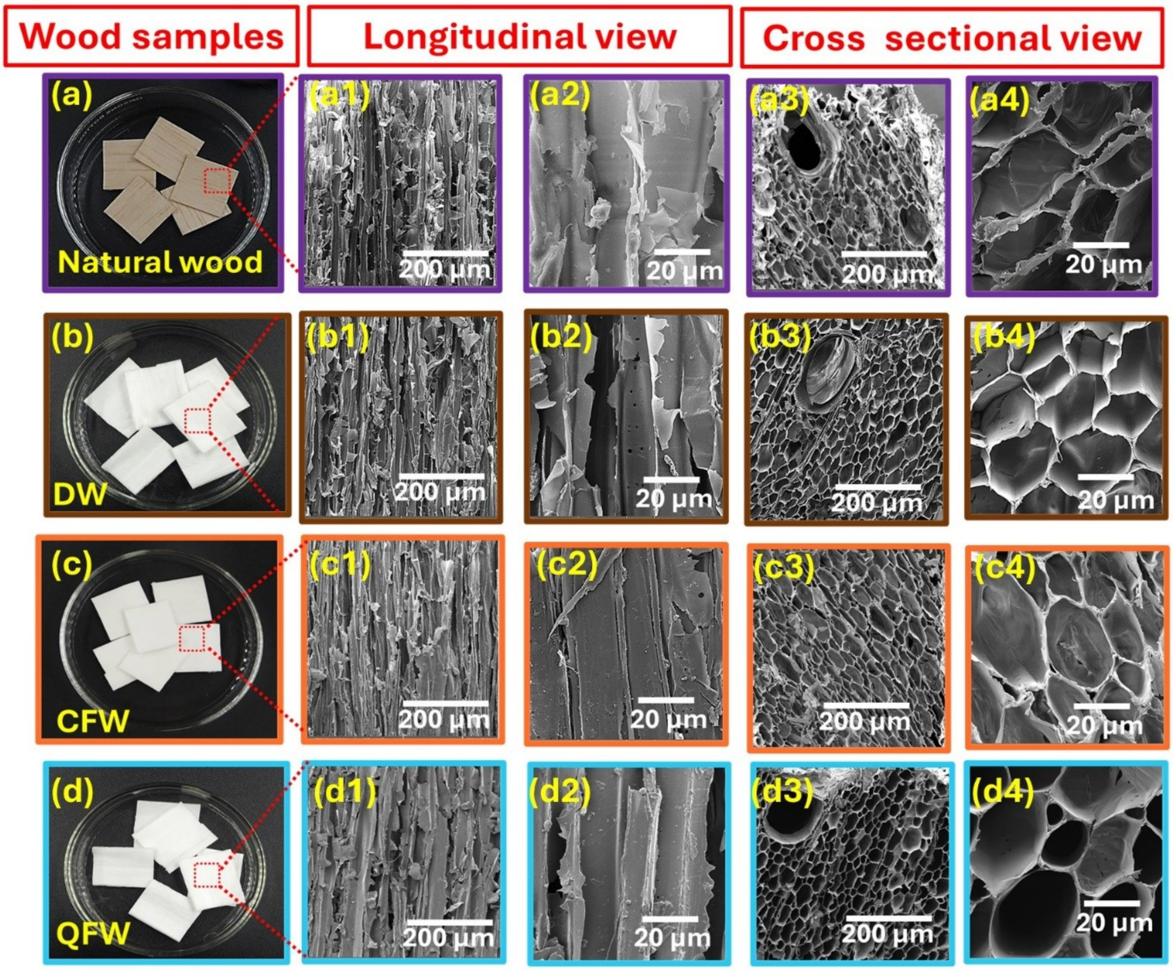

Fig. S5. Morphologies of different wood samples. (a) Digital photograph of natural wood with corresponding FESEM image at different magnifications: (a1-a2) longitudinal view, (a3-a4) cross-sectional view. (b) Digital photograph of delignified wood with corresponding FESEM image at different magnifications: (b1-b2) longitudinal view, (b3-b4) cross-sectional view. (c) Digital photograph of carboxylate functionalized wood with corresponding FESEM image at different magnifications: (c1-c2) longitudinal view, (c3-c4) cross-sectional view. (d) Digital photograph of quaternized functionalized wood with corresponding FESEM image at different magnifications (d1-d2) longitudinal view, (d3-d4) cross-sectional view.

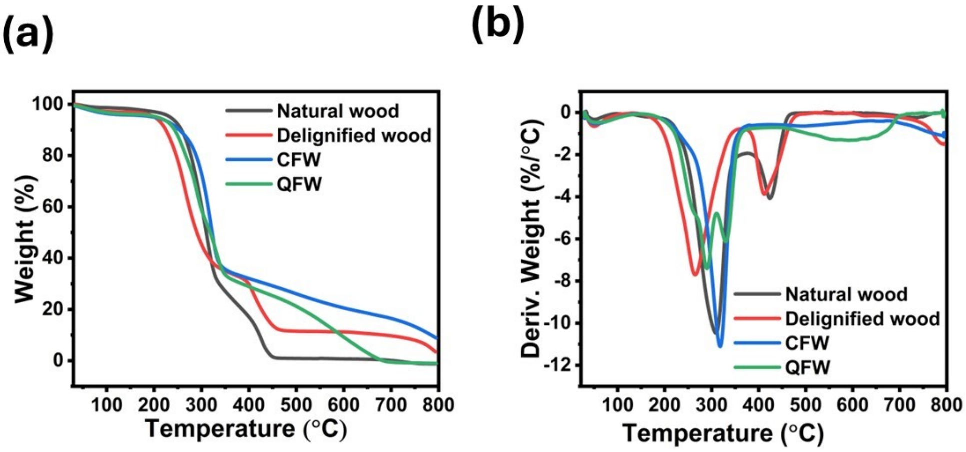

Fig. S6. (a) Thermogravimetric analysis (TGA) curves and (b) Derivative Thermogravimetry (DTG) curves of natural wood, delignified wood, CFW and QFW.

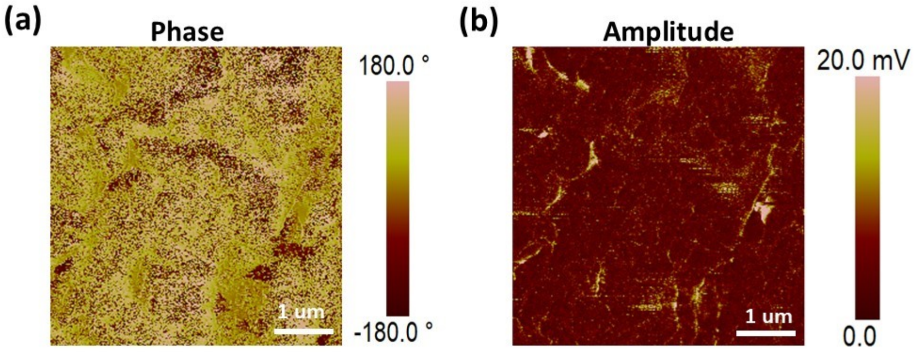

Fig. S7. PFM images (a) Phase and (b) Amplitude image of delignified wood.

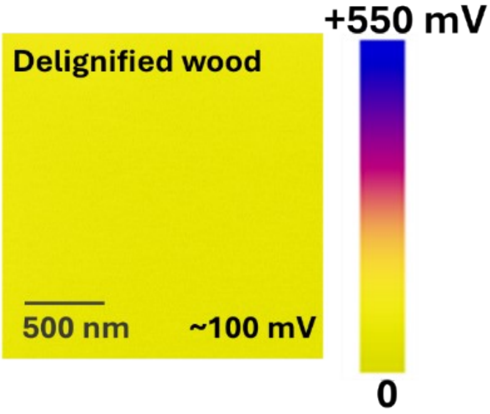

Fig. S8. Kelvin probe force microscopy (KPFM) image of delignified wood showing the surface potential of 100 mV.

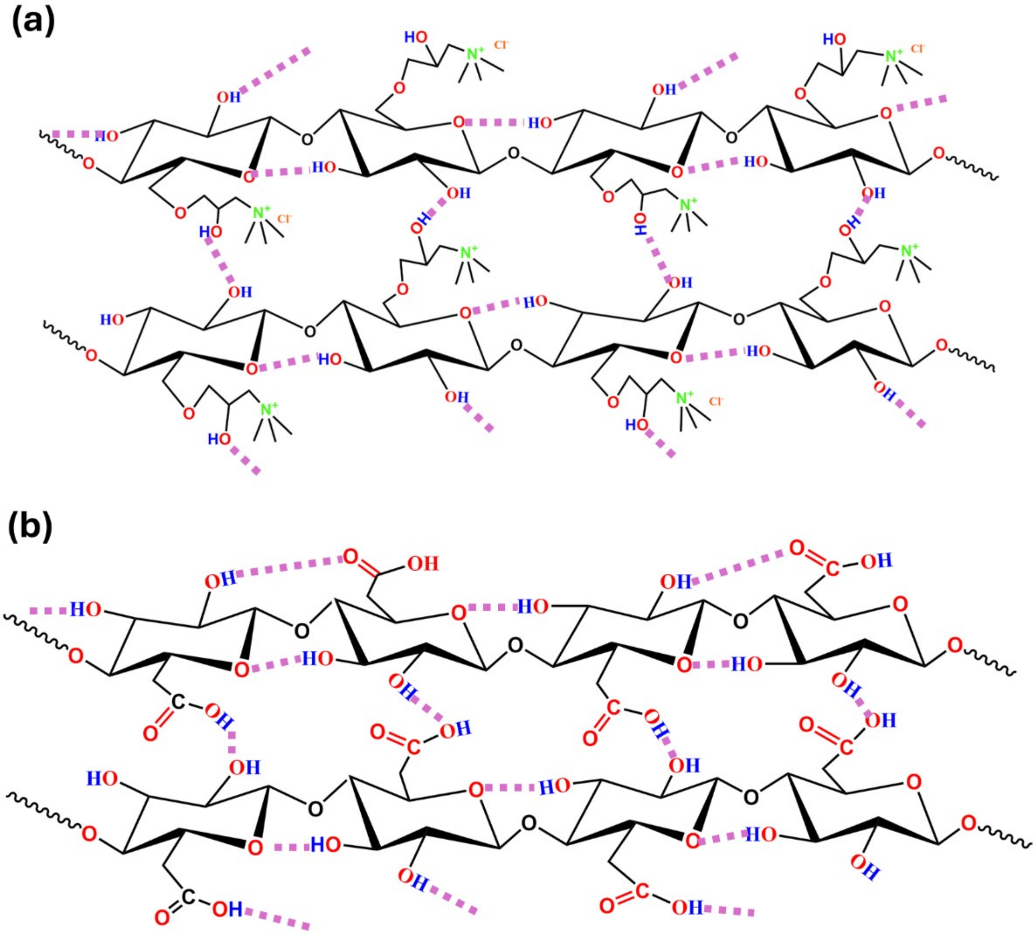

Fig. S9. Illustration of intramolecular and intermolecular H-bonding in (a) quatern functionalized wood and (b) carboxylate functionalized wood.

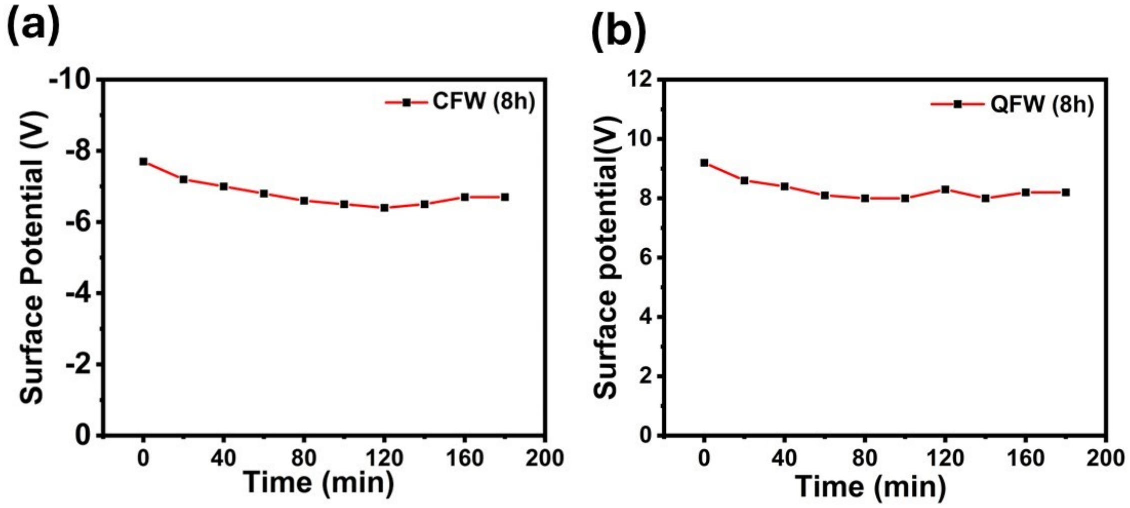

Fig. S10. Change in surface potential with time of (a) CFW (8h) and (b) QFW (8h) measured by electrostatic meter.

Note S3. Equation for potential difference and the short circuit charge

The output voltage of the BFW-NG is governed by Supplementary equation 1, while the corresponding short-circuit charge is defined by Supplementary equation 2. In these equations, V_{oc} refers the open-circuit voltage, and Q_{sc} denotes the short-circuit charge. Here, σ refers to the surface charge density induced on the, A denotes the effective contact area between the interacting triboelectric layers (CFW and QFW), and C_0 denotes the device's capacitance.

$$V_{oc} = -\frac{\sigma A}{2C_o} \qquad 1$$

$$Q_{sc} = -\frac{\sigma A}{2} \qquad 2$$

Note S4. Theoretical simulation of BFW-NG using COMSOL Multiphysics

COMSOL Multiphysics simulations were employed to visualize the spatial distribution of electric potential and to gain deeper insight into the energy-generation mechanism arising from the interaction between quaternized and carboxylate functionalized delignified wood layers during the contact-separation process. The simulations were further used to estimate the expected output voltage of the device, as presented in Fig. 4c. The diagram uses different colors to show variations in electron and hole density within the triboelectric pair. COMSOL simulations indicate that contact electrification occurs upon layer separation, while electrostatic induction develops progressively as the separation distance increases from 0 to 5 mm. In the COMSOL simulations of the BFW-NG, the vertical separation between the opposing triboelectric layers (y_1) was varied from 0 to 5 mm, while the thickness of each layer was fixed at 1.0 mm. As y_1 increases, the electric potential shows a continuous rise, indicating enhanced charge separation. At a separation distance of 5 mm, the electric potential reaches a maximum value of approximately 150 V. These results confirm that the separation distance between the triboelectric layers plays a key role in determining the output voltage of the BFW-NG.

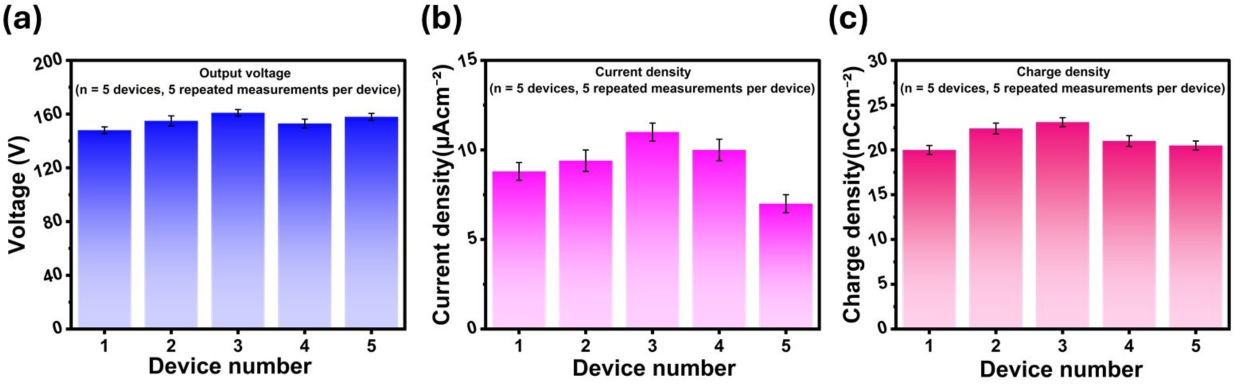

Fig. S11. Statistical analysis of (a) output voltage, (b) current density and (c) charge density measurements obtained from five independent experimental runs (n = 5) under operating conditions of 4Hz and 40N, demonstrating good reproducibility of BFW-NG.

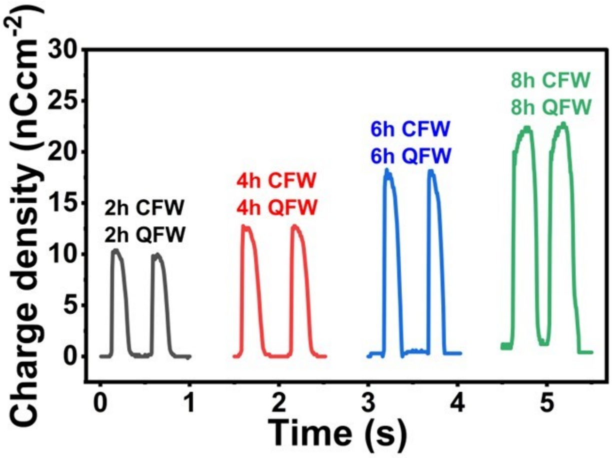

Fig. S12. Functionalization-dependent surface charge density during contact–separation cycles for pristine wood (DW/DW) and chemically functionalized wood (CFW/QFW) at different reaction times (2-8 h).

Note S5. A systematic comparison of the electrical performance of the control TENG

To decouple and quantitatively evaluate the contribution of each component, a systematic set of control experiments was conducted under identical operating conditions (4 Hz, 40 N). The delignified wood TENG utilizing delignified wood as both the layer (DW/DW) and without using the ionic wood as current collector establishes the intrinsic triboelectric baseline of the porous cellulose matrix without chemical functionalization or ionic conduction and exhibits the lowest open circuit voltage (Voc), short-circuit current (Isc), and maximum output power (Pmax), confirming that delignification alone provides limited triboelectric enhancement (Fig. S13 a, Fig. S13 b and Fig. S13 c). In contrast, the functionalized non-ionic TENG utilizing CFW and QFW as triboelectric positive and negative layer respectively (CFW/QFW) without using the ionic wood as current collector pronounced increase in Voc and transferred charge density relative to DW/DW, demonstrating that covalently introduced -COO- and -N+ functional groups enhance surface polarization and charge trapping effects. However, the output power remains significantly lower than that of the fully integrated device, indicating restricted charge transport efficiency in the absence of ionic conduction (Fig. S13 d to Fig. S13 f).

The non-functionalized ionic TENG (IW/IW), where delignified wood is used as both the triboelectric layers and ionic wood as current collector, exhibits an output voltage of approximately 15 V (Fig. S13g). This output arises from ion migration and electric double-layer (EDL) capacitance associated with the LiCl-PVA ionic collector, with the corresponding current density and power density shown in Fig. S13h and Fig. S13i. The characteristic thickness of the EDL can be described by the Debye length (λ_D), which for a symmetric electrolyte is given by

$$\lambda_D = \sqrt{\frac{\varepsilon_r \varepsilon_0 k_B T}{2 N_A C\, e^2}}$$

Where ε_r is the relative permittivity of the ionic medium, ε_0 is the vacuum permittivity, $k_B$is the Boltzmann constant, T is the absolute temperature, N_A is the Avogadro number, C is the molar concentration of the electrolyte (mol m^{-3}), and e is charge of electron.

Using a LiCl concentration of 0.1 M, temperature (≈300 K), and a relative permittivity of $\varepsilon_r \approx 40$ for the hydrated PVA-LiCl-delignified wood medium, λ_D is estimated to be 0.7 nm which is approximate to 1nm. This length scale is much smaller than the characteristic pore size of the delignified wood (~17 µm), indicating that EDL formation is confined to regions near the pore walls, while the pore interior remains available for ion transport. As a result, the IW/IW device shows a finite but comparatively low output voltage, consistent with ionic wood primarily facilitating charge transport and charge collection rather than acting as the main source of voltage generation.

These results collectively demonstrate that the comparative control studies indicate that the major contribution to the enhanced open-circuit voltage originates from chemical functionalization of the triboelectric layers, whereas the ionic conductor plays a secondary role by facilitating charge transport and collection rather than serving as the primary source of voltage generation.

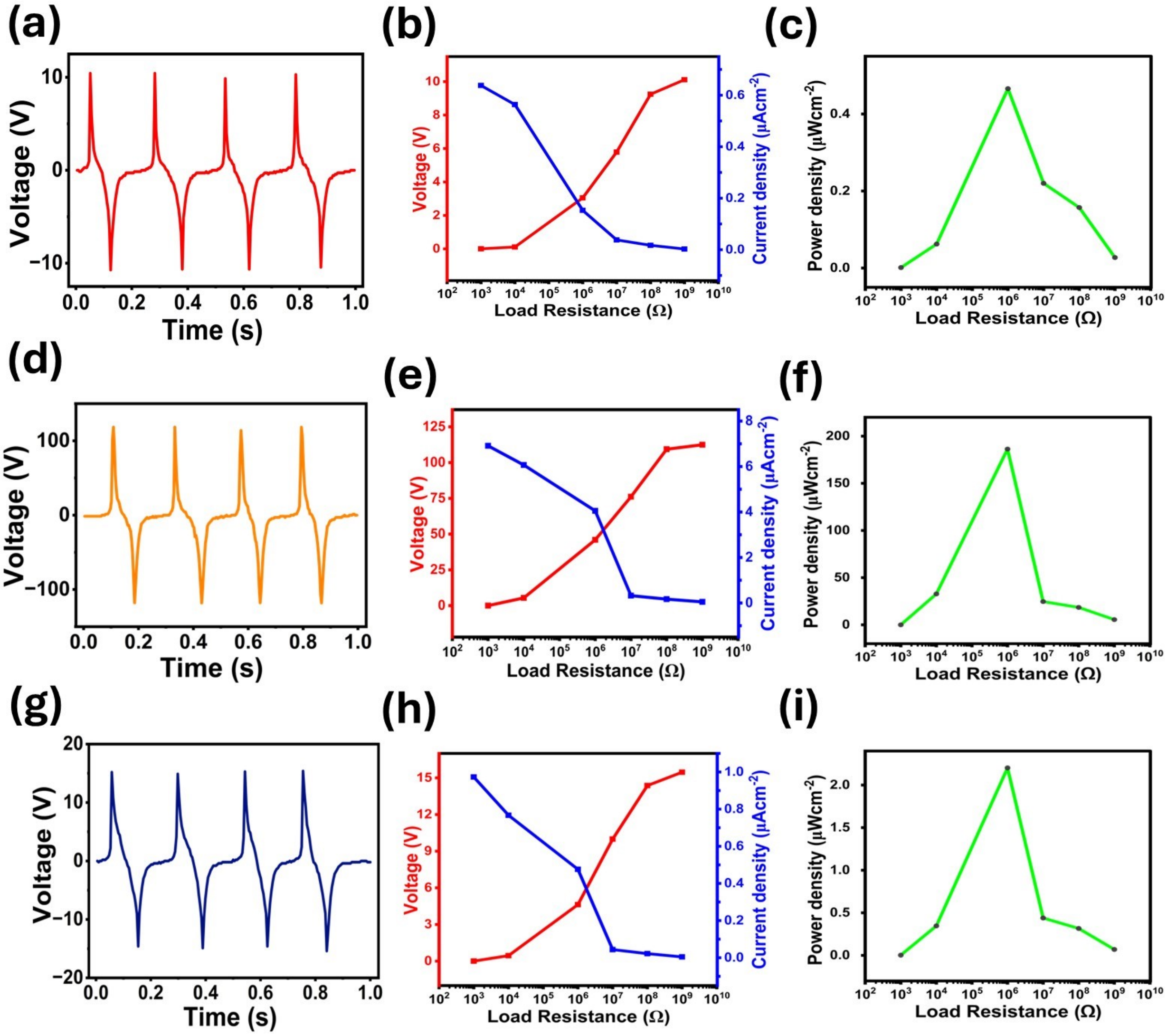

Fig. S13**.** A systematic comparison of the electrical performance of the control TENG configurations under identical conditions (40 N, 4 Hz). The DW/DW device (a) Output voltage (b) voltage and current density variation as a function of resistance (c) power density variation as a function of resistance. The CFW/QFW device (d) Output voltage (e) voltage and current density variation as a function of resistance (f) power density variation as a function of resistance. The IW/IW device (g) Output voltage (h) voltage and current density variation as a function of resistance (i) power density variation as a function of resistance.

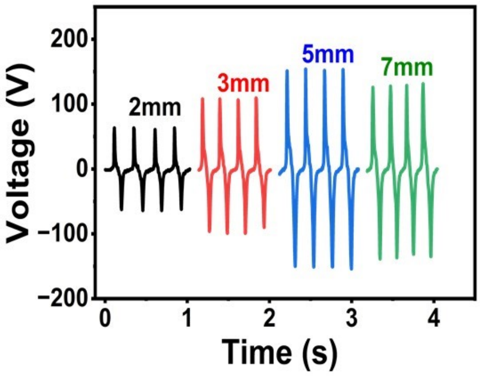

Fig. S14. Effect of separation distance (gap) of the tribolayers QFW and CFW on the output voltage of the TENG under contact-separation mode.

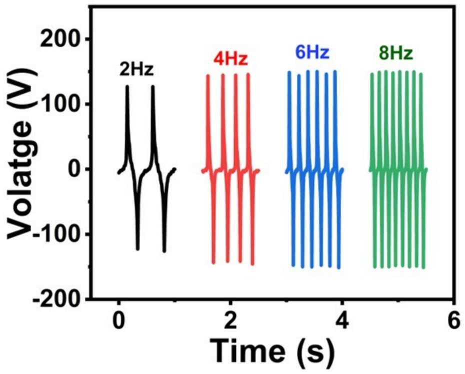

Fig. S15. Output voltage of the BFW-NG at different operating frequencies.

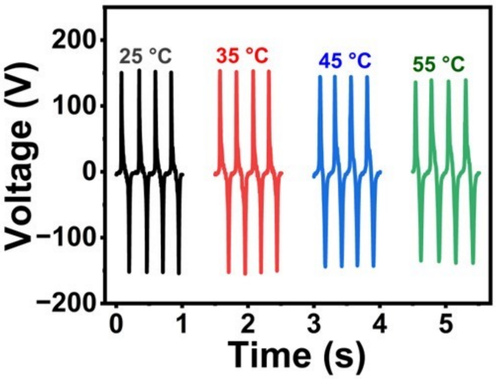

Fig. S16. Output voltage of the BFW-NG at different operating temperatures.

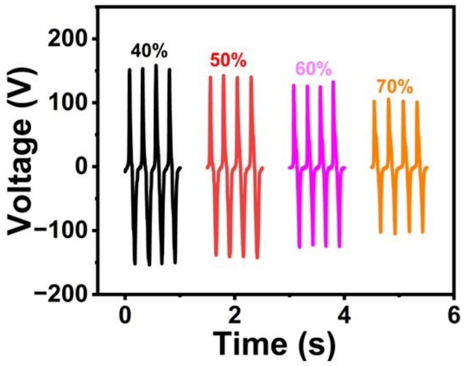

Fig. S17. Output voltage of the BFW-NG at different operating humidity condition.

Table S3. Comparison of output performance of BFW-NG with other degradable material based TENGs.

S. No.	**Material**	**Trigger conditions**	**Voltage**	**Current**	**Power**	**Reference**
1	PLLGA and PCL	Frequency: 1Hz Force: NA	40 V	1 µA	NA	1
2	Calcium alginate film and SA film	Force: NA Frequency: 4Hz	33 V	150 nA	9.5 µW	2
3	PLLA fibres and chitosan	Force: 8 N Frequency: NA	45 V	9 µA	6.5 mWm^{-2}	3

4	Au-doped PLGA film, and Poly(1,8 octanediol-co-citric acid)	Force: NA Frequency: NA	28 V	220 nA	NA	4
5	Zwitterionic Network Hydrogel	Force: NA Frequency: 5Hz	123 V	5.1 μA	209 mWm^{-2}	5
6	PTFE and polyimide and Porous wood	Force: NA Frequency: 4Hz	46.7 V	1.5 μA	0.6 mW	6
7	BC and CNTs and PPy	Force: 6N Frequency: 3Hz	29 V	0.6 μA,	3 μW	7
8	χ-carrageenan-agar, PCL, χC-Agar	Force 10 N Frequency: NA	30 V	0.45 μA cm^{-2}	0.015 μW cm^{-2}	8
9	poly-ε-caprolactone and ethyl cellulose	Force:11 N Frequency: 9 Hz	50 V	6 μA	157.17 mWm^{-2}	9
10	silk fibroin and rice paper	Force: NA Frequency:	55 V	0.6 μA,	21.6 mWm^{-2}	10

		1Hz				
11	Silk nanoribbon film and magnesium	Force: 50 N Frequency: 5Hz	41.64 V	0.5 µA	86.7 mWm^{-2}	11
12	Polyvinyl alcohol and SA	Force: NA Frequency: NA	1.47 V	3.9 nA,	3.8 mWm^{-2}	12
13	silk fibroin and PCL/graphene oxide	Force: 13 N Frequency: 3Hz	100 V	3.15 mA m^{-2}	72 mWm^{-2}	13
14	Starch paper	Force: NA Frequency: NA	11.2 V	1 µA	3.8 µW	14
15	Chitosan with Acetic acid	Force: NA Frequency: NA	13.5V	42 nA	17.5 µWm^{-2}	15
16	PLGA and PVA	Force: 40 N Frequency: 5Hz	90 V	1.5 µA	130 mWm^{-2}	16
17	**CFW and QFW**	**Force: 40N** **Frequency: 4Hz**	**155 V**	**9.4 µAcm^{-2}**	**202.38 µWcm^{-2}**	**This work**

PLLGA: poly(l-lactide-co-glycolide); PCL: poly(caprolactone); SA: Sodium alginate; PLLA: Poly-L-lactic acid; PLGA: polylactic-co-glycolic acid; RC: recycled cellulose; PBAT: poly (butylene adipate-co-terephthalate); GCP: graphene composite paper; PTFE: poly tetra fluoroethylene; BC: bacterial cellulose; CNTs: carbon nanotubes; PPy: polypyrrole: PVA: Polyvinyl alcohol; PBS: phosphate buffer saline; CFW: carboxylate functionalized wood; QFW: quatern functionalized wood; NA: not applicable

References

1 Q. Zheng, Y. Zou, Y. Zhang, Z. Liu, B. Shi, X. Wang, Y. Jin, H. Ouyang, Z. Li and Z. L. Wang, *Sci Adv*, DOI:10.1126/sciadv.1501478.

2 Y. Pang, F. Xi, J. Luo, G. Liu, T. Guo and C. Zhang, *RSC Adv*, DOI:10.1039/c7ra13294h.

3 G. Khandelwal, G. Min, X. Karagiorgis and R. Dahiya, *Nano Energy*, DOI:10.1016/j.nanoen.2023.108325.

4 Z. Li, H. Feng, Q. Zheng, H. Li, C. Zhao, H. Ouyang, S. Noreen, M. Yu, F. Su, R. Liu, L. Li, Z. L. Wang and Z. Li, *Nano Energy*, DOI:10.1016/j.nanoen.2018.10.020.

5 X. Guo, F. Yang, X. Sun, Y. Bai, G. Liu, W. Liu, R. Wang and X. He, *Adv Funct Mater*, DOI:10.1002/adfm.202201230.

6 S. Bi, X. Han, Q. Chen, B. Gao, L. Chen, Z. He and C. Jiang, *Adv Mater Technol*, DOI:10.1002/admt.202201066.

7 J. Zhang, S. Hu, Z. Shi, Y. Wang, Y. Lei, J. Han, Y. Xiong, J. Sun, L. Zheng, Q. Sun, G. Yang and Z. L. Wang, *Nano Energy*, DOI:10.1016/j.nanoen.2021.106354.

8 M. Kang, M. S. B. M. Khusrin, Y.-J. Kim, B. Kim, B. J. Park, I. Hyun, I. M. Imani, B.-O. Choi and S.-W. Kim, *SSRN Electronic Journal*, DOI:10.2139/ssrn.4089526.

9 C. Fan, J. Huang, A. Mensah, Z. Long, J. Sun and Q. Wei, *Cell Rep Phys Sci*, DOI:10.1016/j.xcrp.2022.101012.

10 W. Jiang, H. Li, Z. Liu, Z. Li, J. Tian, B. Shi, Y. Zou, H. Ouyang, C. Zhao, L. Zhao, R. Sun, H. Zheng, Y. Fan, Z. L. Wang and Z. Li, *Advanced Materials*, DOI:10.1002/adma.201801895.

11 Q. Niu, L. Huang, S. Lv, H. Shao, S. Fan and Y. Zhang, *Nano Energy*, DOI:10.1016/j.nanoen.2020.104837.

12 Q. Liang, Q. Zhang, X. Yan, X. Liao, L. Han, F. Yi, M. Ma and Y. Zhang, *Advanced Materials*, DOI:10.1002/adma.201604961.

13 S. Parandeh, M. Kharaziha, F. Karimzadeh and F. Hosseinabadi, *Nanotechnology*, DOI:10.1088/1361-6528/ab9972.

14 Z. Zhu, K. Xia, Z. Xu, H. Lou and H. Zhang, *Nanoscale Res Lett*, DOI:10.1186/s11671-018-2786-9.

15 R. Wang, S. Gao, Z. Yang, Y. Li, W. Chen, B. Wu and W. Wu, *Advanced Materials*, DOI:10.1002/adma.201706267.

16 X. Peng, K. Dong, C. Ye, Y. Jiang, S. Zhai, R. Cheng, D. Liu, X. Gao, J. Wang and Z. L. Wang, *Sci Adv*, DOI:10.1126/sciadv.aba9624.